

## SOLAR CELLS

# Triple-halide wide-band gap perovskites with suppressed phase segregation for efficient tandems

Jixian Xu<sup>1,2,3\*</sup>†, Caleb C. Boyd<sup>2,4†</sup>, Zhengshan J. Yu<sup>5</sup>, Axel F. Palmstrom<sup>2</sup>, Daniel J. Witter<sup>1,2</sup>, Bryon W. Larson<sup>2</sup>, Ryan M. France<sup>2</sup>, Jérémie Werner<sup>1,2</sup>, Steven P. Harvey<sup>2</sup>, Eli J. Wolf<sup>2,4</sup>, William Weigand<sup>5</sup>, Salman Manzoor<sup>5</sup>, Maikel F. A. M. van Hest<sup>2</sup>, Joseph J. Berry<sup>2</sup>, Joseph M. Luther<sup>2</sup>, Zachary C. Holman<sup>5</sup>, Michael D. McGehee<sup>1,2,6\*</sup>

Wide-band gap metal halide perovskites are promising semiconductors to pair with silicon in tandem solar cells to pursue the goal of achieving power conversion efficiency (PCE) greater than 30% at low cost. However, wide-band gap perovskite solar cells have been fundamentally limited by photoinduced phase segregation and low open-circuit voltage. We report efficient 1.67-electron volt wide-band gap perovskite top cells using triple-halide alloys (chlorine, bromine, iodine) to tailor the band gap and stabilize the semiconductor under illumination. We show a factor of 2 increase in photocarrier lifetime and charge-carrier mobility that resulted from enhancing the solubility of chlorine by replacing some of the iodine with bromine to shrink the lattice parameter. We observed a suppression of light-induced phase segregation in films even at 100-sun illumination intensity and less than 4% degradation in semitransparent top cells after 1000 hours of maximum power point (MPP) operation at 60°C. By integrating these top cells with silicon bottom cells, we achieved a PCE of 27% in two-terminal monolithic tandems with an area of 1 square centimeter.

Compositional tuning can yield optoelectronic properties of state-of-the-art ABX<sub>3</sub> metal halide perovskites that are desirable for use in highly efficient solar cells, light-emitting diodes (LEDs), and detectors. Such tuning has been achieved through mixing of cations such as methylammonium (MA), formamidinium (FA), cesium (Cs), dimethylammonium (DMA), and methylenediammonium (MDA) at the A site (1–6); lead (Pb) and tin (Sn) at the B site (7, 8); and iodine (I) and bromine (Br) at the X site (9, 10). Wide-band gap alloys (>1.65 eV) in particular are of considerable interest for both LEDs and multijunction solar cells (11–13). The latter can overcome the Shockley-Queisser limit of single-junction cells by stacking complementary wide-band gap and narrow-band gap absorbers to reduce thermalization losses (11, 14). As market-dominant silicon solar cells approach their theoretical limit of 29.1% with a lab record of 26.7% (15, 16), the development of multijunction solar cells or tandem solar cells could help to further increase the power conversion efficiency (PCE) and reduce the leveled cost of photovoltaic (PV) electricity (17, 18).

Although a range of band gaps from 1.6 to 3.06 eV can be achieved through I/Br and Br/Cl alloying (9, 10, 19–21), wide-band gap alloys in the optimum range for use in tandem solar cells suffer from short diffusion lengths and photoinduced phase segregation, which lead to poor optoelectronic qualities and substantial open-circuit voltage ( $V_{oc}$ ) deficits relative to their theoretical limit (12, 22, 23). Studies of this unexpectedly large  $V_{oc}$  deficit revealed photoinduced trap formation by halide segregation, especially when the Br fraction on the X-site was >20% (12, 22, 23). The alloyed I/Br phases segregated upon illumination and photocarriers were funneled into the low-band gap I-rich domains, which acted as traps that redshift the photoluminescence and reduce the  $V_{oc}$  (23). Reduced photoinduced phase segregation and improved material quality of wide-band gap perovskites through cation substitution of Cs or DMA achieve wide band gaps while limiting the Br fraction (2, 24, 25). Additive engineering can reduce defect densities (26–30). Surface engineering techniques such as the formation of 2D/3D heterostructures have also been used for improving device  $V_{oc}$  (31). However, wide-band gap solar cells still are in need of both a reduced  $V_{oc}$  deficit and improved photostability (13).

Inspired by recent advances in achieving improved material quality with triple- or quadruple-cation perovskites (1, 6) and reports suggesting that Cl as an additive may reduce defect density (32–35), we explored the triple-halide (I, Br, Cl) compositional space. Generally, previous studies have reported the use of Cl as an additive or precursor to affect morphology and surface passivation but with little or no incorporation into the bulk material. The Cl also had little

impact on the band gap, independent of the Cl ratio included in the precursor (33–40). The lack of incorporation into the bulk lattice with little change in the band gap occurs because Cl typically volatilizes as MACl or FACl during annealing of the perovskite film and only acts to control film crystallization, as it resides at grain boundaries or on perovskite film surfaces in the final material.

We report that Cs and Br act as a bridge to a new phase space in wide-band gap perovskites of triple-halide alloys containing I, Br, and Cl at molar amounts >15%. We directly incorporated Cl into the lattice at much larger amounts than previously reported, observing a uniform halide distribution throughout the material with a reduction in lattice parameter and an increase in band gap corresponding to increasing amounts of Cl in the lattice. By extending the double-halide to triple-halide alloy, we observed a distinct enhancement in optoelectronic characteristics, such as factor of 2 increases in photocarrier lifetime and mobility and the suppression of light-induced phase segregation at intensities up to 100 suns. These material advances reduced the  $V_{oc}$  deficit of 1.67-eV wide-band gap solar cells by 100 mV and boosted PCE from ~18% to 20.3% (Table 1 and table S1). We demonstrated large-area (1 cm<sup>2</sup>), wide-band gap semitransparent top cells for Si tandems with a high certified performance of 16.83% that resulted from a substantially improved  $V_{oc}$  relative to prior reports (Table 1 and table S2). The triple-halide material was also operationally stable in solar cells that maintained >96% of their initial efficiency after 1000 hours of maximum power tracking under white light illumination at 60°C, and >97% of their initial efficiency after 500 hours at 85°C. By integrating triple-halide semitransparent top cells with Si bottom cells with PCE of ~21% (41), we boosted their PCE by 30%, to 27% in 1-cm<sup>2</sup> two-terminal monolithic tandems (Table 1 and table S3).

## Alloying chlorine into the perovskite lattice

We started with a targeted perovskite band gap of ~1.67 eV, which is in the range of ideal top-cell band gaps for a perovskite/Si tandem, taking into account imperfect absorption near the band edge (42, 43). FA<sub>0.75</sub>Cs<sub>0.25</sub>Pb(I<sub>0.8</sub>Br<sub>0.2</sub>)<sub>3</sub> has a band gap of 1.67 eV and was recently demonstrated to enable 25% PCE in two-terminal perovskite/Si tandems (25). We denote this perovskite family as CsFA perovskite, and denote this composition as Cs25Br20 in accordance with the percentage of Cs at the A site and the percentage of Br at the X site. Cs25Br20 outperformed its 1.67-eV counterpart Cs17Br25 in light stability and  $V_{oc}$  deficit, attributed to the reduced Br fraction and increased Cs fraction. To further improve the photostability, we reduced the Br fraction to 15% and found that Cs25Br15 has a band gap

<sup>1</sup>Chemical and Biological Engineering, University of Colorado, Boulder, CO 80309, USA. <sup>2</sup>National Renewable Energy Laboratory, Golden, CO 80401, USA. <sup>3</sup>CAS Key Laboratory of Materials for Energy Conversion, Department of Materials Science and Engineering, University of Science and Technology of China, Hefei 230026, China. <sup>4</sup>Materials Science and Engineering, Stanford University, Stanford, CA 94305, USA. <sup>5</sup>School of Electrical, Computer, and Energy Engineering, Arizona State University, Tempe, AZ 85281, USA. <sup>6</sup>Materials Science and Engineering, University of Colorado, Boulder, CO 80309, USA.

\*Corresponding author. Email: michael.mcgehee@colorado.edu (M.D.M.); jixianxu@ustc.edu.cn (J.X.)

†These authors contributed equally to this work.

of ~1.63 eV. To recover the optimal 1.67-eV band gap, we attempted to increase the Cs fraction but obtained lower PV performance (25), consistent with recent reports that a high Cs fraction might lead to halide inhomogeneity and phase segregation (4, 44).

We sought to raise the band gap by alloying MAPbCl<sub>3</sub> perovskite into the lattice of CsFA perovskites. We chose MAPbCl<sub>3</sub> perovskite because it has a wide band gap (2.88 eV) and higher stability than its Br and I counterparts (45, 46). When we mixed Cs25Br15 with 2 to 5 mol % MAPbCl<sub>3</sub> (referred to hereafter as Cs25Br15+Cl2 and Cs25Br15+Cl5) in solution, the band gap of the resulting films could be continuously raised from 1.63 to >1.67 eV (Fig. 1A and fig. S1). The sharp onset of the external quantum efficiency (EQE) indicated that a photoactive triple-halide perovskite phase had formed.

We used x-ray diffraction (XRD) to verify the triple-halide phase and determine the lattice constant. As indicated by the shift of the diffraction peaks (figs. S2 and S3), the perovskite single phase was retained and the lattice constant continually decreased with increasing MAPbCl<sub>3</sub> fraction. Specifically, Cs25Br15+Cl5 has a lattice constant of ~6.24 Å (Fig. 1F), which is similar to that of Cs25Br20 and evidently less than that of the host perovskite Cs25Br15, 6.27 Å.

Incorporating Cl into perovskite precursor solutions has been widely reported to increase the size of apparent grain domains in solid films, because the formation and outgassing of MACl modify the nucleation and crystal growth dynamics (47–51). Prior reports showed that the band gap remained substantially unchanged and that the Cl concentrations in the solid films were below the detection limit of energy-dispersive x-ray spectrometry (EDX) and x-ray photoelectron spectroscopy (XPS), even though a large portion of Cl was present in the precursors (33, 34, 36). In contrast, we did not observe enlargement of grain domains when more Cl was incorporated into the triple-halide films, as shown by scanning electron microscope (SEM) images (Fig. 1B and fig. S4).

In addition, we could readily detect Cl using XPS. The Cl-to-Pb ratio of films also increased when a higher fraction of Cl was included in

the precursors (fig. S5). The Cl in the triple-halide films was uniformly distributed throughout the entire film thickness, similar to I and Br, as shown by time-of-flight secondary ion mass spectrometry (TOF-SIMS) depth profiling (Fig. 1C). To mitigate measurement artifacts (52), we recorded secondary ion clusters or molecular ion signals of Cs<sub>2</sub>Cl<sup>+</sup>, Cs<sub>4</sub>I<sub>3</sub><sup>+</sup>, and Cs<sub>2</sub>Br<sup>+</sup> to track the depth profile of halides. The relative scaling of SIMS profiles between halides did not represent their stoichiometric ratio (53).

Taken together, the EQE, XRD, SEM, XPS, and SIMS observations show that Cl was incorporated into the perovskite lattice and increased its band gap, rather than being sacrificed as a volatile phase. Because the lattice constant of the host perovskites was reduced by the Cs and Br, Cl was closer to the ideal size for the X-site in the lattice. This explanation is consistent with the formation of MAPbBr/Cl perovskites being more thermodynamically preferred than MAPbI/Cl double-halide alloys (19–21).

Because perovskites with even wider band gaps are needed for all-perovskite tandems and possibly other applications, we identified the phase boundary of the triple-halide alloying strategy and obtained additional mechanistic insights into the perovskite phase space. When we further increased the molar ratio of Cl/(I+Br+Cl) to above 10% in Cs25Br15, we observed an inflection point in the band gap evolution curve (Fig. 1D, red line). That is, the band gap of the films began to decrease with increased Cl content, as shown in the EQE spectra (fig. S1). This increasing and then decreasing of the band gap with triple-halide alloying is anomalous and distinctly different from the monotonic growth trend reported in I/Br double-halide alloys (9, 10, 23).

Structural evolution observed with XRD (Fig. 1, E and F, and fig. S2) revealed that the band gap decrease at high Cl content was caused by phase segregation into two perovskite phases. At the phase boundary, the diffraction peaks of a segregated phase (very likely MAPbCl<sub>x</sub>Br<sub>3-x</sub>) emerged (fig. S2, A and D). The lattice of the host perovskite then expanded (diffraction peaks shifted to lower angles) with the growth of the segregated perovskite phase (Fig. 1F, red line, and fig. S2D), consistent with the ob-

served band gap decrease and suggesting the segregation of a high-Br/Cl phase, which left behind an I-rich, lower-band gap host perovskite (Fig. 1D and fig. S1).

To further validate the generality of the triple-halide alloy, we also used Cs25Br30 and Cs25Br40 as the host perovskites to investigate the evolution of band gap (see EQE data in figs. S6 and S7) and lattice constant (see XRD data in figs. S8 and S9) when increasing the triple-halide alloy ratio. The trends in the band gap (Fig. 1D) and lattice constant (Fig. 1F) were consistent, further substantiating this mechanism of triple-halide alloying. In all cases, the band gap-raising rate was ~0.0078 eV, with each percent of Cl alloyed to form the single phase. The inflection point of band gap evolution (or the phase boundary between the single-phase triple-halide alloy and phase segregation) consistently increased with increased Br content, as in Cs25Br15, Cs25Br30, and Cs25Br40, indicating a wider single-phase range and greater tolerance to phase segregation in the perovskite with higher Br content. This finding verified that Br reduced the alloy barrier between I and Cl phases for triple-halide alloys. The addition of PbCl<sub>2</sub> in Cs25Br15 also increased the band gap in a manner similar to the effect of adding MAPbCl<sub>3</sub> (fig. S10), thereby reconfirming that Cl incorporation is the determinant to the band gap raising in triple-halide alloys. Adding MACl alone did not raise the band gap (fig. S10A), in agreement with previous reports that MACl volatilizes during film annealing (47–51).

Improved optoelectronic properties of triple-halide perovskites

Recent studies showcase the improvements in optoelectronic properties that result from incorporating even small amounts of Cl (<1%) (32–34, 47, 50). For example, small Cl ions might reduce the halogen vacancy defect density and improve the stability of perovskites in ambient air (32). Given that in our triple-halide perovskites, Cl-based reagents are well incorporated into the lattice, we used time-resolved microwave conductivity (TRMC) to study their electronic properties and charge-carrier dynamics (54). Despite no increase in apparent grain size in the triple-halide perovskites (Fig. 1B), an enhancement in both the charge-carrier

Table 1. PV parameters of solar cells using 1.67-eV triple-halide wide-band gap perovskites. Area is defined by optical aperture placed in front of devices.

Cell configuration	Area (cm <sup>2</sup> )	V <sub>oc</sub> (V)	J <sub>sc</sub> (mA cm <sup>-2</sup> )	FF (%)	PCE (%)	Stabilized PCE (%)
Opaque single-junction	0.06	1.217	20.18	83.16	20.42	20.32
Top-illumination semitransparent	0.34	1.214	19.13	80.21	18.59	18.53
Top-illumination semitransparent	1	1.202	18.99	74.07	16.90	16.83* (certified)
Two-terminal tandem on Si	1	1.886	19.12	75.3	27.13	27.04

\*11-point stabilized power output (SPO) measurement.

mobility and lifetime by nearly a factor of 2, equivalent to a doubled carrier diffusion length, was seen in comparison to our best 1.67-eV controls. Specifically, when the absorbed photon flux was  $\sim 1 \times 10^{10} \text{ cm}^{-2}$  (near 1-sun intensity), the lifetime increased from 420 to 846 ns (Fig. 2A) and the charge-carrier mobility improved from 29 to 53  $\text{cm}^2 \text{ V}^{-1} \text{ s}^{-1}$  (Fig. 2B).

To disentangle the effect of Cl incorporation on the bulk and surface, we applied a passivating layer on top of the perovskite to reduce surface recombination. We chose LiF because it is insulating and suppresses nonradiative surface recombination in perovskites, thereby increasing the carrier effective lifetime (55). In TRMC measurements, LiF-capped perovskite samples exhibited the same mobility and lifetime as bare perovskite samples (Fig. 2), which confirmed that the enhancement in photo-carrier transport in triple-halide perovskites is

dominated by the bulk properties rather than surfaces. Given that there was no increase of grain size, we assert that the harmful defect density for carriers is greatly reduced by Cl incorporation in triple-halide films. Dark microwave conductivity measurements showed a factor of 2 reduction (from  $7.8 \times 10^{15} \text{ cm}^{-3}$  to  $2.9 \times 10^{15} \text{ cm}^{-3}$ ) in dark carrier density (fig. S11), confirming the reduced defect density in triple-halide perovskites over the control. Taking into account both the potential contribution of defects to photoinstability (26–30) and the reduced Br ratio in triple-halide perovskites, we expected that the photoinduced phase segregation would also be reduced.

To compare the susceptibility of triple-halide films and our best Cs25Br20 controls to light-induced phase segregation, we carried out time- and intensity-dependent photoluminescence (PL) measurements under 488-nm continuous-

wave laser illumination in a  $\text{N}_2$  environment. A red shift or a lower-energy peak forming in the PL spectrum indicates the formation of light-induced low-band gap I-rich trap states, as seen in previous reports (23, 25, 28, 30, 56). Here, to avoid noise and error in peak position, we used the spectral centroid to quantitatively indicate the evolution of the population spanning the entire PL spectral range. During the course of 20 min at 10-sun-equivalent illumination, Cs25Br20 controls exhibited low-energy PL peaks and increasing peak width (Fig. 3A). In contrast, 1.67-eV triple-halide films showed no low-energy peak formation and retained their PL spectral profile, highlighting their superior photostability (Fig. 3D). At an ultra-high injection level of 100 suns, the red shift and broadening of the PL peak became more apparent in Cs25Br20 controls (Fig. 3B), consistent with previous reports. Surprisingly, we

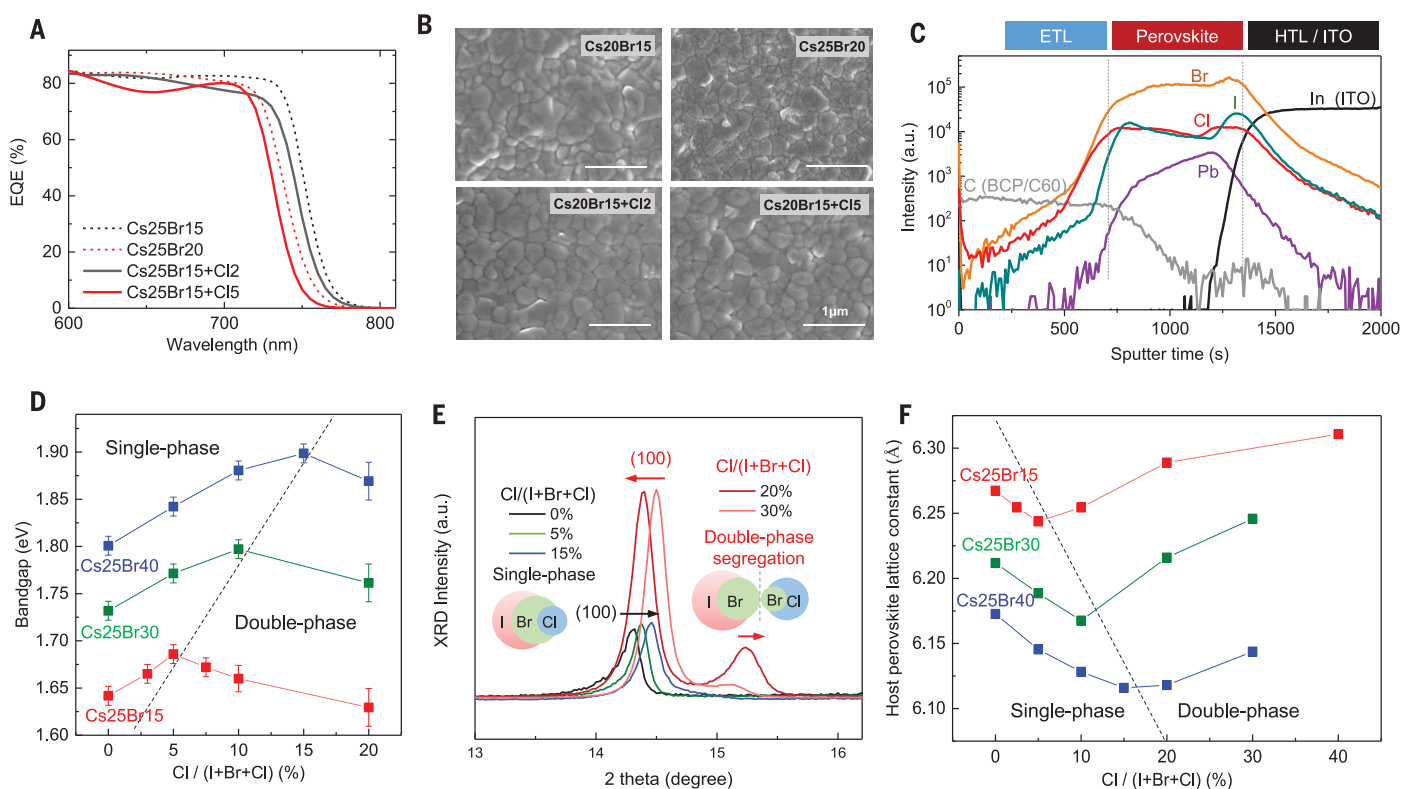


**Fig. 1. Characteristics of triple-halide perovskite alloys.** (A) EQE measurements show the band gap raising via the formation of triple-halide perovskites with 2 to 5 mol % Cl relative to host perovskites. Cs25Br15 and Cs25Br20 denote the double-halide perovskites  $\text{Cs}_{0.25}\text{FA}_{0.75}\text{Pb}(\text{I}_{0.85}\text{Br}_{0.15})_3$  and  $\text{Cs}_{0.25}\text{FA}_{0.75}\text{Pb}(\text{I}_{0.8}\text{Br}_{0.2})_3$ , respectively. Cs25Br15+Cl2 and Cs25Br15+Cl5 denote the triple-halide perovskites with an additional 2 or 5 mol %  $\text{MAPbCl}_3$  included in the Cs25Br15, respectively. (B) Top-view SEM images show no evident difference of apparent grain size between triple-halide perovskites and double-halide control films. (C) TOF-SIMS depth profiles show the uniform distribution of halides throughout the entire film thickness of the triple-halide perovskite (Cs25Br15+Cl5). Here, the Cs trace is not included because a Cs ion beam was used for sputtering to increase halide signal intensities, which makes the Cs profile through the device stack difficult to interpret. The secondary ion clusters or molecular ion signals of  $\text{Cs}_2\text{Cl}^+$ ,  $\text{Cs}_4\text{I}_3^+$ , and  $\text{Cs}_2\text{Br}^+$  were recorded to

track the depth profile of halides. The relative scaling of SIMS profiles between halides does not represent their stoichiometric ratio. ETL (electron transport layer) is a stack of  $\text{C}_{60}/\text{BCP}$  layers. (D) Evolution curves of band gap for triple-halide films with increased ratio of Cl/(I+Br+Cl), based on Cs25Br15 (red), Cs25Br30 (green), and Cs25Br40 (blue), respectively. The dashed line delineates the single-phase and double-phase zones corresponding to band gap raising and band gap reducing, respectively. Error bars denote SD. (E) Shifting and splitting of XRD (100) peaks shows the transition from single-phase triple-halide alloy to double-phase segregation with increased Cl content. Here, the host perovskite is Cs25Br40. The intensity of XRD peaks is rescaled for ease of peak position comparison. (F) Evolution curves of host perovskite lattice constant with increasing ratios of Cl/(I+Br+Cl). The dashed line delineates the single-phase and double-phase zones corresponding to band gap raising and band gap reducing, respectively.



observed a PL blue shift, rather than a red shift, in triple-halide films caused by the emission growth at the PL high-energy shoulder (Fig. 3E). This opposite trend was also observed in the traces of the spectral centroid over time (Fig. 3, C and F).

This PL blue shift of wide-band gap perovskites at a high injection level is unusual and strongly suggests that incorporation of Cl into the lattice had an impact on the optoelectronic properties and halide phase-segregation pathways. Our TRMC and PL data suggested a combination of mechanisms: (i) the Moss-Burstein effect in the phase-stabilized semiconductors, which originates from the lifting of the quasi-Fermi level when the conduction band edge is fully populated at a high injection level (57, 58), and (ii) a decrease in defect concentration.

### Efficient and stable triple-halide perovskite/silicon tandems

To evaluate the effect of doubled charge-carrier diffusion length and better photo-stability in triple-halide films, we fabricated 1.67-eV single-junction solar cells with opaque metal contacts. We used a p-i-n structure (Fig. 4A): glass / indium tin oxide (ITO) / poly(4-butylphenyl-diphenyl-amine) (poly-TPD) / poly(9,9-bis(3'-(*N,N*-dimethyl)-*N*-ethylammonium-propyl-2,7-fluorene)-alt-2,7-(9,9-dioctylfluorene)) dibromide (PFN-Br) / perovskite / LiF /  $C_{60}$  / bathocuproine (BCP) / Ag. The statistical comparison of devices (fig. S12) showed that triple-halide devices performed better than our best Cs25Br20 controls for all PV metrics. The best-performing triple-halide device with composition Cs22Br15+Cl3 (Fig. 4B) exhibited a PCE of 20.42% and  $V_{oc}$  of 1.217 V [ $J_{sc}$  = 20.18 mA cm<sup>-2</sup>, fill factor (FF) = 83.16%, active area = 0.06 cm<sup>2</sup>], whereas the best-performing control showed a PCE of 18.16% and  $V_{oc}$  of 1.114 V. Both the control and triple-halide devices exhibited no hysteresis in  $J$ - $V$  sweeps. By integrating the EQE spectrum, weighted by the AM1.5G solar spectrum (Fig. 4G), we calculated a current density of 20.6 mA cm<sup>-2</sup>, in good agreement with the  $J_{sc}$  obtained in the  $J$ - $V$  test. The stabilized efficiency was 20.32% after continuous operation at MPP for 5000 s (Fig. 4C). Table S1 summarizes reported p-i-n wide-band gap cells for tandems (2, 24, 47, 54, 59, 60). The triple-halide devices considerably improved the  $V_{oc}$  deficit, which was reduced from >0.5 V to ~0.45 V, as well as the PCE, which increased to >20%.

To construct tandems on top of Si cells, we developed top-illuminated semitransparent devices that maximized both the near-infrared transparency and PV performance. The device structure is illustrated in Fig. 4D. The metal top contact (Ag or Au) in opaque cells was replaced with an 8-nm-thick SnO<sub>2</sub> / Zn:SnO<sub>2</sub> (ZTO) buffer layer (2, 41, 54, 61, 62) coated by atomic-layer deposition (ALD) and an ITO win-

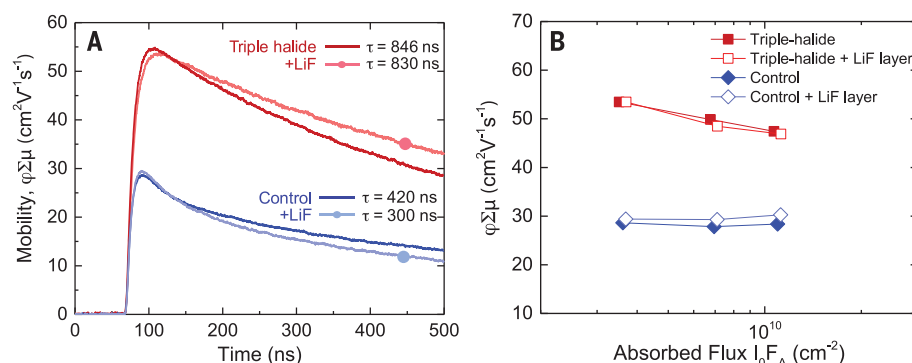


**Fig. 2. Enhanced charge-carrier mobility and lifetime in triple-halide perovskite films.** (A) Photoconductivity transient (indicative of the lifetime) measured by time-resolved microwave conductivity (TRMC), indicating doubled charge-carrier lifetime ( $\tau$ ) in the 1.67-eV triple-halide film (Cs22Br15+Cl3, red line) compared with the control film (Cs25Br20, blue line). (B) Photoconductivity under different excitation intensity.  $\phi \Sigma \mu$  denotes the yield-mobility product. The carrier-generation yield  $\phi$  is near unity for perovskite films and therefore  $\phi \Sigma \mu$  is a measure of mobility. Triple-halide films exhibit nearly doubled mobility relative to control double-halide films. Perovskite/LiF bilayer samples exhibit mobilities and lifetimes similar to their corresponding bare perovskite samples.

dow layer to allow light through. Parasitic absorption and reflection loss created by layers in the top electrode were minimized (fig. S13) by using a polydimethylsiloxane (PDMS) scattering layer to limit reflection (67) and by reducing the thickness of the  $C_{60}$  and ITO layers to 10 and 60 nm, respectively (fig. S14).

To reduce the resistance of large-area devices, we evaporated a metal grid on top of the ITO window layer. Note that in top-illuminated devices,  $J_{sc}$  is typically lower than the EQE integrated current density because of the shading losses created by the metal grid. To minimize this loss, we used a metal shadow mask with a graded opening to reduce the shadow effect that occurs when metals are evaporated through high-aspect ratio holes in a mask (fig. S15). The graded-opening mask enabled us to construct ~25- $\mu$ m-wide metal gridlines with a height of ~3  $\mu$ m using thermal evaporation (fig. S16), which reduced the shading loss to below 0.8% without compromising FF.

With these improvements, our 1.67-eV top-illuminated semitransparent cells simultaneously achieved ~80% near-infrared transmittance (Fig. 4G) and PCEs of 18.59% (Fig. 4E). The corresponding stabilized PCE was 18.52% in the MPP tracking test (Fig. 4E, inset). The  $V_{oc}$  of 1.214 V and FF of 80.2% in 0.34-cm<sup>2</sup> semitransparent devices were near those achieved in the best 0.06-cm<sup>2</sup> opaque devices with a metallic electrode (Fig. 4B and Table 1), highlighting the quality and stability of triple-halide perovskites during ALD buffer layer deposition at 85°C and subsequent ITO sputter deposition. The active-area  $J_{sc}$  determined from the EQE spectrum (Fig. 4G) was ~19.5 mA cm<sup>-2</sup>, which agrees well with the aperture-area  $J_{sc}$  of 19.13 mA cm<sup>-2</sup> from  $J$ - $V$  tests. The loss of  $J_{sc}$  in semitransparent top cells relative to opaque de-

vices primarily resided in the long-wavelength region around the band edge and arose from the lack of reflection from the metal contact.

We also fabricated large-area (1 cm<sup>2</sup>) semitransparent top cells. One such device was measured by an accredited PV laboratory (National Renewable Energy Laboratory PV Device Performance) and certified at a stabilized PCE of 16.83 ± 0.34% in an 11-point SPO (stabilized power output) test. This value appears to be the highest certified PCE reported for a 1-cm<sup>2</sup> semitransparent perovskite cell for tandems (table S2 and figs. S17 and S18). The performance metrics of the  $J$ - $V$  curve were  $V_{oc}$  = 1.202 V,  $J_{sc}$  = 18.99 mA cm<sup>-2</sup>, FF = 74.07%, and PCE = 16.90% (Fig. 4F and Table 1). The nearly identical PCEs measured in a  $J$ - $V$  test and SPO test further verified the negligible hysteresis and stability of our triple-halide perovskite devices. The primary PCE loss in the large-area (1 cm<sup>2</sup>) devices relative to small-area (0.34 cm<sup>2</sup>) devices resided in FF, which is attributed to the limited sheet resistance (15 ohms per square) of ITO substrates used in this study; this limitation does not apply to two-terminal tandems that transport current vertically through the recombination layer between the top and bottom cells. Our semitransparent top cells exhibited both the highest PCE and highest  $V_{oc}$  of reported semitransparent top cells for tandems on Si, CIGS (copper indium gallium diselenide), or narrow-band gap perovskites (table S2) (24, 41, 54, 60, 63–72).

We examined the long-term operational stability of triple-halide devices under the combined stresses of heating and illumination (~0.77-sun sulfur plasma lamp, chamber temperature  $T$  = 60°C; see supplementary materials for details). An unencapsulated opaque device with metal contacts tested in ambient

air (relative humidity = 25 to 30%) retained 90% of its initial PCE after 250 hours of continuous operation at MPP (Fig. 4H). The thermal stability of the triple-halide material was also tested by keeping opaque devices with gold contacts at 85°C for 500 hours in nitrogen; the unencapsulated triple-halide devices and double-halide devices both retained >97% of their initial efficiency (fig. S19). Semitransparent top cells tested in N<sub>2</sub> exhibited negligible degradation (<4%) after 1000 hours of continuous operation at MPP near 60°C (Fig. 4H). This result confirmed the importance of encapsulation (N<sub>2</sub> in this case) and the role of barrier layers [an ALD buffer layer and a transparent conductive oxide (TCO) layer in this case] to suppress the reactions between metal contacts and halides, as revealed in previous reports (73–75).

We integrated our triple-halide perovskite in 1-cm<sup>2</sup> two-terminal monolithic tandems on silicon cells (see photos in fig. S20). Here, the ITO/glass substrate of the semitransparent device (Fig. 4D) was replaced by a front-side polished silicon heterojunction bottom cell

capped with a 20-nm-thick ITO recombination layer, which allowed for solution processing of the perovskite layer rather than vapor deposition that would be required to deposit the perovskite on a pyramidally textured silicon surface (65, 76). With the aid of proper light management, tandems on planar front-side wafers have been shown to deliver  $J_{sc}$  values competitive with those on fully textured wafers (77). Additionally, front-side planar substrates are industrially relevant, because PERC (passivated emitter and rear cell) silicon cells, which constitute ~70% of the silicon PV market, have a planar “shiny-etched” rear surface that was recently shown to allow for solution processing of the perovskite solar cell (78).

The full tandem structure is illustrated in Fig. 5A. Figure 5B shows a cross-sectional SEM image of the perovskite top cell on Si. Here, we developed a NiO<sub>x</sub>/poly-TPD bilayer hole transport layer (HTL) for use in the tandems. Relative to HTLs that used only spin-cast poly-TPD, introducing a 20-nm-thick sputtered NiO<sub>x</sub> layer between the ITO-HTL interface reduced

shunting and increased the yield of 1-cm<sup>2</sup> tandems. In a  $J$ - $V$  sweep, the best-performing tandem reached a PCE of 27.13% ( $V_{oc}$  = 1.886 V,  $J_{sc}$  = 19.12 mA cm<sup>-2</sup>, and FF = 75.3%). The corresponding stabilized PCE at MPP is 27.04% (Fig. 5C and Table 1), exceeding the current record efficiency (26.7%) for Si single cells and approaching the world record value of 28% achieved by Oxford PV (15, 16). The  $V_{oc}$  of >1.88 V is one of the highest reported in perovskite/Si tandems with PCE of >25% (59, 61, 65, 76, 77) (see summary of ≥1 cm<sup>2</sup>-area tandems in table S3), providing further evidence of the low  $V_{oc}$  deficit achieved in the triple-halide semitransparent top cells (table S2). The EQE spectrum of the perovskite top cell matches well with those measured in top-illumination semitransparent devices (Fig. 5D). The active-area  $J_{sc}$  values calculated from the EQE spectra were 19.3 mA cm<sup>-2</sup> and 19.9 mA cm<sup>-2</sup> for the perovskite top cell and Si bottom cell, respectively (Fig. 5D). These calculated values indicate that the  $J_{sc}$  of our two-terminal tandem was slightly limited by the perovskite top cell.

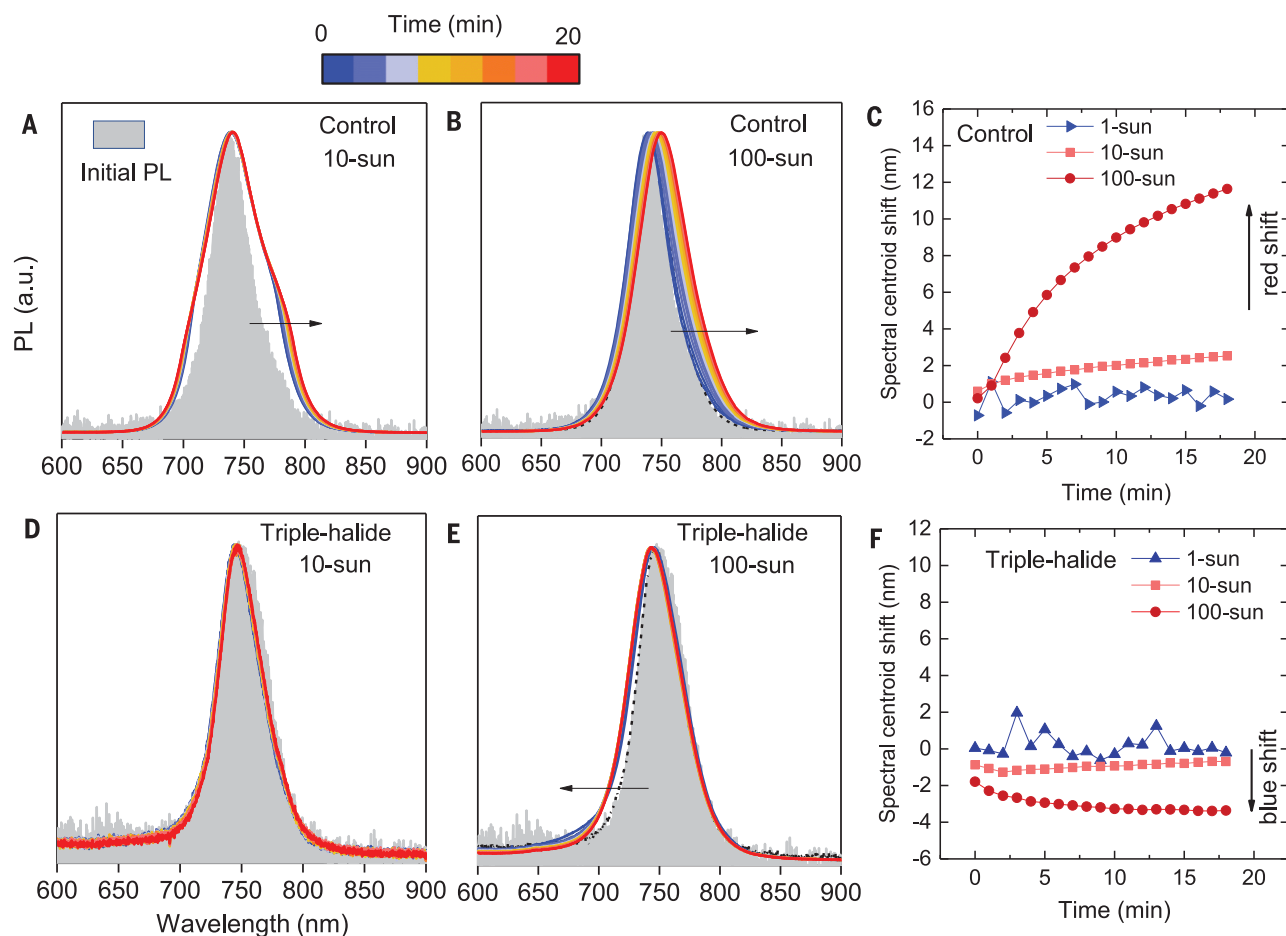


**Fig. 3. Suppression of photoinduced phase segregation in triple-halide perovskites.** (A and B) PL spectra of 1.67-eV control perovskite films (Cs<sub>25</sub>Br<sub>20</sub>) under 10-sun and 100-sun illumination for 20 min, respectively. Arrows indicate the direction of the PL shift over time. (C) The shift of the spectral centroids of control films over time. The red shift becomes more obvious under higher injection. (D and E) PL spectra of 1.67-eV triple-halide perovskites (Cs<sub>22</sub>Br<sub>15</sub>+Cl<sub>3</sub>) under 10-sun and 100-sun illumination for 20 min, respectively. (F) The shift of the spectral centroids of triple-halide perovskites over time. The blue shift becomes more obvious under higher injection level.

We also analyzed each subcell in our two-terminal tandems by measuring electroluminescence (EL) (Fig. 5E). After increasing the injection current density from  $1 \text{ mA cm}^{-2}$  to  $100 \text{ mA cm}^{-2}$ , the EL peak from the perovskite retained its shape and location, verifying the phase stability of triple-halide perovskites (Fig. 5F). The subcell's  $V_{oc}$  was estimated from EL quantum efficiency based on the reciprocity

principle (Fig. 5G) (79). At an injection level of 17 to  $20 \text{ mA cm}^{-2}$  (near  $J_{sc}$  and  $J_{mpp}$ ), the respective  $V_{oc}$  values of the perovskite and Si subcells were estimated to be 1.2 V and 0.7 V, aligning well with the tandem  $V_{oc}$  of  $\sim 1.9 \text{ V}$  from  $J$ - $V$  measurements.

A two-terminal tandem device was certified after being tested in air and stored in  $N_2$  for 1 month (figs. S21 and S22). The certified

efficiency (25.8%) is highly consistent with that measured in our lab (26%) (fig. S21A), verifying our rigorous protocol of in-house tandem measurement. From the comparison of EQE spectra (fig. S21B), the  $J_{sc}$  loss relative to our champion tandem (Fig. 5D) is likely caused by the absorption from a thicker  $C_{60}$  top layer, as discussed above (figs. S13 and S14). Even with this  $J_{sc}$  loss, it exhibited a  $V_{oc}$  value

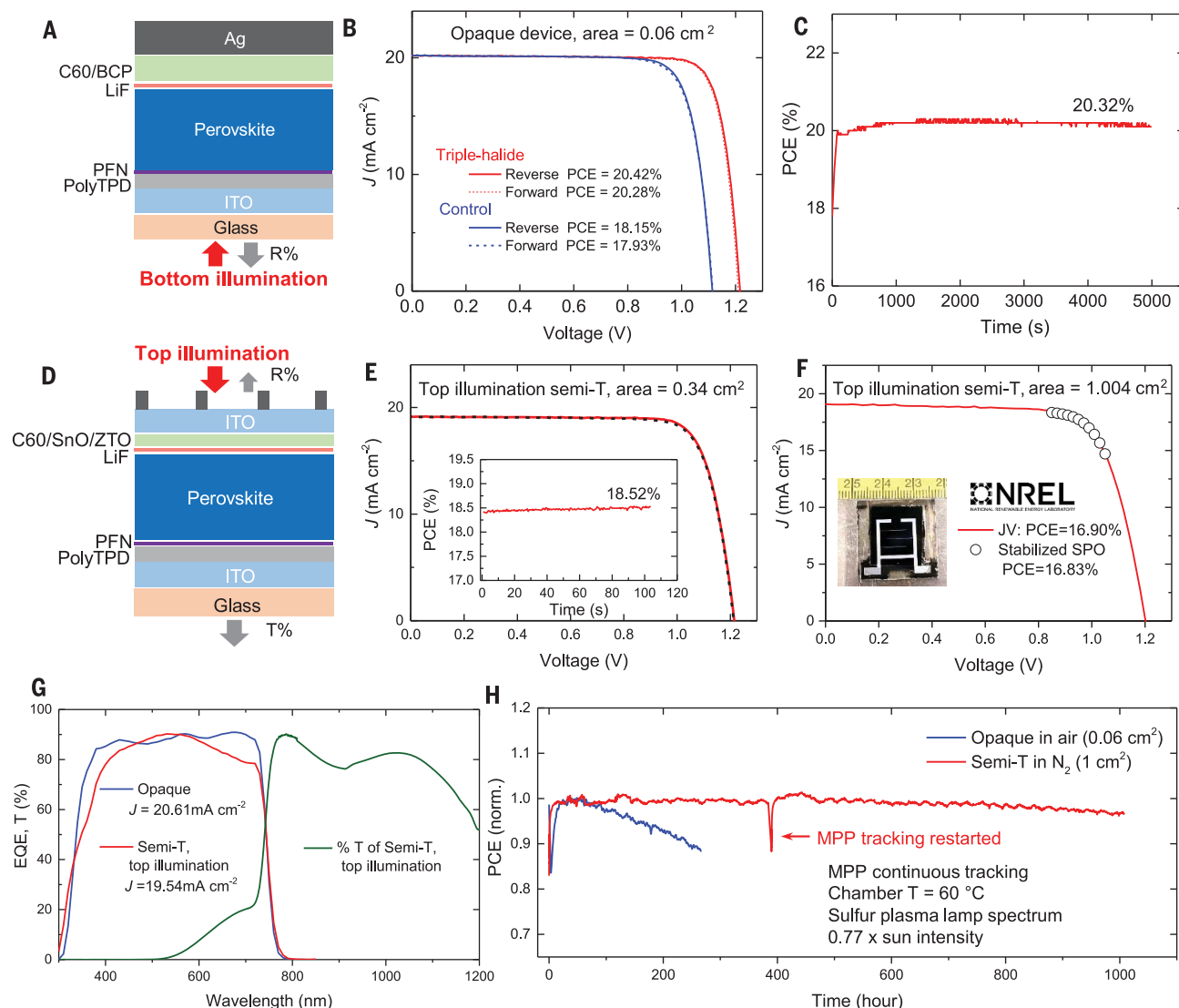


**Fig. 4. PV characteristics of single-junction opaque devices and semitransparent top cells.** (A) Schematic of the opaque device with reflective metal contact (not to scale). (B)  $J$ - $V$  curves of the champion 1.67-eV triple-halide opaque device (red) and best control device (blue). The aperture area is  $0.06 \text{ cm}^2$ . Solid lines indicate the reverse scan (from open circuit to short circuit); dashed lines indicate the forward scan (from short circuit to open circuit). (C) Continuous maximum-power-point (MPP) operation of the champion triple-halide wide-band gap device for 5000 s, exhibiting stabilized PCE of 20.32%. (D) Schematic of the top-illuminated semitransparent device (not to scale). Light enters the cell through the top metal grid and TCO layer. (E)  $J$ - $V$  curves of the champion semitransparent device illuminated from the

top metal grid and TCO layer side. The aperture area is  $0.34 \text{ cm}^2$ . The inset shows continuous MPP operation for 100 s, exhibiting stabilized PCE of 18.52%. (F) A  $1\text{-cm}^2$  top-illuminated semitransparent device certified by NREL. The circles are the 11-point SPO (stabilized power output) measurements, showing stabilized PCE of 16.83%. The  $J$ - $V$  curve shows the instantaneous PCE of 16.90%; the inset is a photo of the device. (G) EQE spectra of an opaque device (blue) and a top-illuminated semitransparent device (red). The green curve is the optical transmission of the top-illuminated semitransparent device, including the metal grid shading losses. (H) Long-term continuous MPP tracking under accelerated conditions (0.77-sun illumination and  $60^\circ\text{C}$ ) of  $1\text{-cm}^2$  semitransparent (red, tested in  $N_2$ , averaged from two devices in the same batch) and opaque devices (blue, tested in air with relative humidity of  $\sim 30\%$ ).

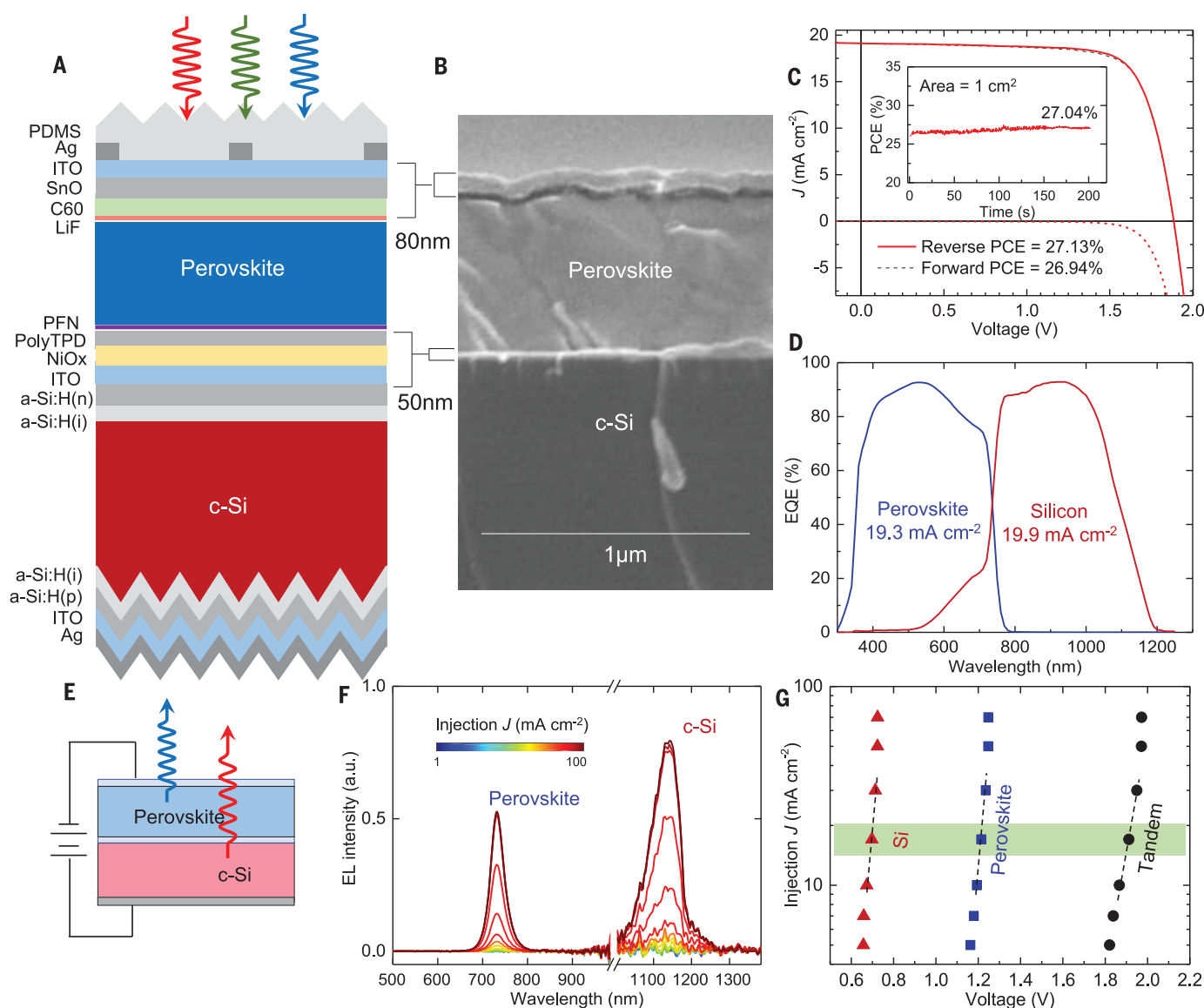


**Fig. 5. PV characteristics of 1-cm<sup>2</sup> two-terminal perovskite/Si tandems.**

(A) Schematic of the two-terminal monolithic tandem structure (not to scale). a-Si:H denotes hydrogenated amorphous silicon. (B) Cross-sectional SEM image of a two-terminal tandem. (C) Light and dark  $J$ - $V$  curves and MPP tracking (inset) of the champion tandem. (D) EQE spectra of the perovskite top cell (blue) and silicon bottom cell (red) of the champion tandem. (E) Schematic

diagram of electroluminescence (EL) measurement of a two-terminal tandem.

(F) EL spectra of the tandem under different injection levels. The triple-halide perovskite exhibits a stable EL peak up to injection levels of 100 mA cm<sup>-2</sup>.

(G) The  $V_{oc}$  contribution of each subcell estimated from EL quantum efficiency. The injection region of 17 to 20 mA cm<sup>-2</sup> (near  $J_{sc}$  and  $J_{mpp}$  under 1-sun illumination) is highlighted in green.

(1.88 V) that is much improved over the best prior reports (<1.8 V) (table S3). Finally, the statistical data of tandems (fig. S23) indicates that our method was reproducible.

## Outlook

We have demonstrated a low-cost tandem technology to increase the power output of a ~21% silicon solar cell by ~30%, which has major implications given that silicon currently accounts for >90% of the global PV market, which mainly consists of 19 to 21% single-junction silicon solar modules. Furthermore,

triple-halide wide-band gap perovskites offer a promising path to >30% tandems because of their reduced  $V_{oc}$  deficit and record performance in wide-band gap semitransparent top cells. Although we have used a planar tandem architecture as a model in this study, the 1.67-eV, triple-halide perovskite composition also has an ideal band gap for textured perovskite/silicon tandems (80), with potential for a  $J_{sc}$  value of ~20 mA cm<sup>-2</sup>. Both CsPbBr<sub>3</sub>Cl<sub>3-x</sub> perovskites and Cs<sub>m</sub>FA<sub>n</sub>MA<sub>3-m-n</sub>PbI<sub>x</sub>Br<sub>3-x</sub> perovskites with tunable band gaps have been demonstrated by co-evaporation or two-step interdiffusion

methods (65, 76, 81), so there is no fundamental barrier to realizing triple-halide perovskites using vapor deposition methods required for fully textured surfaces. A perovskite/Si tandem with a  $J_{sc}$  of ~20 mA cm<sup>-2</sup> and the  $V_{oc}$  and FF of triple-halide semitransparent cells presented here could have >30% PCE.

The ability to further tune the band gap to higher energies shows promise for other multijunction architectures as well, such as perovskite/perovskite and perovskite/CIGS tandems. Beyond tandems, the demonstrated suppressed photoinduced phase segregation



and improved optoelectronic properties result in stable electroluminescence at high injection current densities and stabilized perovskite PL at 100-sun-equivalent illumination, highlighting opportunities for the use of this material in LED or concentrated PV applications. More broadly, the exploration of triple-halide perovskites has identified a promising new region of perovskite single-phase stability and paves the way for another dimension of compositional engineering for perovskites.

## REFERENCES AND NOTES

- M. Saliba et al., *Energy Environ. Sci.* **9**, 1989–1997 (2016).
- A. F. Palmstrom et al., *Joule* **3**, 2193–2204 (2019).
- G. E. Eperon et al., *Energy Environ. Sci.* **7**, 982–988 (2014).
- Z. Li et al., *Chem. Mater.* **28**, 284–292 (2016).
- H. Min et al., *Science* **366**, 749–753 (2019).
- M. Saliba et al., *Science* **354**, 206–209 (2016).
- F. Hao, C. C. Stoumpos, R. P. H. Chang, M. G. Kanatzidis, *J. Am. Chem. Soc.* **136**, 8094–8099 (2014).
- Y. Ogomi et al., *J. Phys. Chem. Lett.* **5**, 1004–1011 (2014).
- J. H. Noh, S. H. Im, J. H. Heo, T. N. Mandal, S. I. Seok, *Nano Lett.* **13**, 1764–1769 (2013).
- C. M. Sutter-Fella et al., *Nano Lett.* **16**, 800–806 (2016).
- Z. Yu, M. Leilaoui, Z. Holman, *Nat. Energy* **1**, 16137 (2016).
- M. Anaya, G. Lozano, M. E. Calvo, H. Miguez, *Joule* **1**, 769–793 (2017).
- T. Leijtens, K. A. Bush, R. Prasanna, M. D. McGehee, *Nat. Energy* **3**, 828–838 (2018).
- W. Shockley, H. J. Queisser, *J. Appl. Phys.* **32**, 510–519 (1961).
- M. A. Green et al., *Prog. Photovolt. Res. Appl.* **27**, 565–575 (2019).
- K. Yoshikawa et al., *Nat. Energy* **2**, 17032 (2017).
- Z. J. Yu, J. V. Carpenter III, Z. C. Holman, *Nat. Energy* **3**, 747–753 (2018).
- Z. Li et al., *Joule* **2**, 1559–1572 (2018).
- N. Pellet, J. Teuscher, J. Maier, M. Grätzel, *Chem. Mater.* **27**, 2181–2188 (2015).
- C. Li et al., *ACS Appl. Mater. Interfaces* **8**, 11526–11531 (2016).
- D. M. Jang et al., *Nano Lett.* **15**, 5191–5199 (2015).
- E. L. Unger et al., *J. Mater. Chem. A* **5**, 11401–11409 (2017).
- E. T. Hoke et al., *Chem. Sci.* **6**, 613–617 (2015).
- D. P. McMeekin et al., *Science* **351**, 151–155 (2016).
- K. A. Bush et al., *ACS Energy Lett.* **3**, 428–435 (2018).
- M. Abdi-Jalebi et al., *Nature* **555**, 497–501 (2018).
- A. J. Barker et al., *ACS Energy Lett.* **2**, 1416–1424 (2017).
- R. A. Belisle et al., *ACS Energy Lett.* **3**, 2694–2700 (2018).
- S. J. Yoon, M. Kuno, P. V. Kamat, *ACS Energy Lett.* **2**, 1507–1514 (2017).
- W. Rehman et al., *Energy Environ. Sci.* **10**, 361–369 (2017).
- S. Gharibzadeh et al., *Adv. Energy Mater.* **9**, 1803699 (2019).
- M. I. Saidaminov et al., *Nat. Energy* **3**, 648–654 (2018).
- V. L. Pool, A. Gold-Parker, M. D. McGehee, M. F. Toney, *Chem. Mater.* **27**, 7240–7243 (2015).
- S. Colella et al., *Chem. Mater.* **25**, 4613–4618 (2013).
- P.-W. Liang et al., *Adv. Energy Mater.* **5**, 1400960 (2015).
- L. Cojocaru et al., *Chem. Lett.* **44**, 1089–1091 (2015).
- S. Dastidar et al., *Nano Lett.* **16**, 3563–3570 (2016).
- N. Ueoka et al., *AIP Conf. Proc.* **1929**, 020026 (2018).
- T. Oku, Y. Ohishi, H. Tanaka, *AIP Conf. Proc.* **1929**, 020010 (2018).
- J. Jeong et al., *ACS Energy Lett.* **1**, 712–718 (2016).
- K. A. Bush et al., *Nat. Energy* **2**, 17009 (2017).
- M. T. Hörantner, H. J. Snaith, *Energy Environ. Sci.* **10**, 1983–1993 (2017).
- D. A. Jacobs et al., *J. Phys. Chem. Lett.* **10**, 3159–3170 (2019).
- J.-P. Correa-Baena et al., *Science* **363**, 627–631 (2019).
- R. Comin et al., *J. Mater. Chem. C* **3**, 8839–8843 (2015).
- G. Maculan et al., *J. Phys. Chem. Lett.* **6**, 3781–3786 (2015).
- B. Chen et al., *Joule* **3**, 177–190 (2018).
- Y. Zhao, K. Zhu, *J. Phys. Chem. C* **118**, 9412–9418 (2014).
- Q. Dong et al., *Energy Environ. Sci.* **8**, 2464–2470 (2015).
- F. Xie et al., *Energy Environ. Sci.* **10**, 1942–1949 (2017).
- T. Leijtens et al., *Sustain. Energy Fuels* **2**, 2450–2459 (2018).
- S. P. Harvey et al., *ACS Appl. Mater. Interfaces* **11**, 30911–30918 (2019).
- S. P. Harvey et al., *ACS Appl. Mater. Interfaces* **10**, 28541–28552 (2018).
- D. H. Kim et al., *Joule* **3**, 1734–1745 (2019).
- M. Stollerfoht et al., *Nat. Energy* **3**, 847–854 (2018).
- R. E. Beal et al., *J. Phys. Chem. Lett.* **7**, 746–751 (2016).
- E. Burstein, *Phys. Rev.* **93**, 632–633 (1954).
- J. Fu et al., *Nat. Commun.* **8**, 1300 (2017).
- L. Mazzarella et al., *Adv. Energy Mater.* **9**, 1803241 (2019).
- T. Duong et al., *Adv. Energy Mater.* **7**, 1700228 (2017).
- K. A. Bush et al., *ACS Energy Lett.* **3**, 2173–2180 (2018).
- A. F. Palmstrom et al., *Adv. Energy Mater.* **8**, 1800591 (2018).
- J. Tong et al., *Science* **364**, 475–479 (2019).
- J. Werner et al., in *2017 IEEE 44th Photovoltaic Specialist Conference (PVSC)* (2017), pp. 3256–3259.
- F. Sahli et al., *Nat. Mater.* **17**, 820–826 (2018).
- C. O. Ramirez Quiroz et al., *J. Mater. Chem. A* **6**, 3583–3592 (2018).
- J. Werner et al., *ACS Energy Lett.* **1**, 474–480 (2016).
- Q. Han et al., *Science* **361**, 904–908 (2018).
- B. Chen et al., *Adv. Energy Mater.* **6**, 1601128 (2016).
- F. Fu et al., *Nat. Energy* **2**, 16190 (2017).
- J. Peng et al., *Adv. Energy Mater.* **7**, 1601768 (2017).
- H. Shen et al., *Energy Environ. Sci.* **11**, 394–406 (2018).
- C. C. Boyd, R. Cheacharoen, T. Leijtens, M. D. McGehee, *Chem. Rev.* **119**, 3418–3451 (2019).
- C. C. Boyd et al., *ACS Energy Lett.* **3**, 1772–1778 (2018).
- J. A. Raiford et al., *Adv. Energy Mater.* **9**, 1902353 (2019).
- G. Nogay et al., *ACS Energy Lett.* **4**, 844–845 (2019).
- E. Köhnen et al., *Sustain. Energy Fuels* **3**, 1995–2005 (2019).
- Y. Wu et al., in *Proceedings of the Asia-Pacific Solar Research Conference*, [http://apvi.org.au/solar-research-conference/wp-content/uploads/2019/12/43\\_Wu-Yiliang\\_PV\\_2019.pdf](http://apvi.org.au/solar-research-conference/wp-content/uploads/2019/12/43_Wu-Yiliang_PV_2019.pdf) (2019).
- U. Rau, *Phys. Rev. B* **76**, 085303 (2007).
- S. Manzoor et al., *Opt. Express* **26**, 27441–27460 (2018).
- P. Du et al., *ACS Appl. Mater. Interfaces* **11**, 47083–47090 (2019).

## ACKNOWLEDGMENTS

We thank G. Teeter for XPS measurements and A. Hazarika for supporting XRD measurements. **Funding:** This material is based on work supported by the U.S. Department of Energy's Office of Energy Efficiency and Renewable Energy (EERE) under Solar Energy Technologies Office (SETO) agreement number DE-EE0008167. Also supported by the NSF Graduate Research Fellowship under grant DGE-1656518 (C.C.B.); the Office of Naval Research under award number N00014-17-1-2525 (E.J.W.); and the De-risking Halide Perovskite Solar Cells program of the National Center for Photovoltaics, funded by the U.S. Department of Energy, Office of Energy Efficiency and Renewable Energy, Solar Energy Technology Office. Work at the National Renewable Energy Laboratory is supported by the U.S. Department of Energy under contract number DE-AC36-08GO23808. **Author contributions:** M.D.M., Z.C.H., Z.J.Y., J.M.L., and J.J.B. supervised the research; J.X. formed the idea and developed the materials and top cells; J.X. and C.C.B. fabricated and characterized the perovskites and devices; Z.J.Y. and W.W. fabricated the Si bottom cells; A.F.P. developed and deposited ALD buffer layers; S.M. fabricated the PDMS film; D.J.W. and M.F.A.M.v.H. contributed to the development and deposition of TCO layers for tandems; B.W.L. conducted the TRMC measurement; J.W. supported the material and device characterizations; R.M.F. supported the tandem characterizations; S.P.H. conducted the SIMS measurement; E.J.W. supported the stability test; M.D.M., J.X., and C.C.B. wrote the manuscript; and all authors discussed the results and revised the manuscript. **Competing interests:** A.F.P. and M.D.M. are inventors on patent application PCT/US2017/051753 submitted by Stanford University that covers the atomic layer deposition of contacts used in this work. **Data and materials availability:** All data needed to evaluate the conclusions in the paper are present in the paper or the supplementary materials. All the data are available from the corresponding authors upon reasonable request.

## SUPPLEMENTARY MATERIALS

science.sciencemag.org/content/367/6482/1097/suppl/DC1  
Materials and Methods  
Figs. S1 to S23  
Tables S1 to S3  
References (82, 83)

15 September 2019; resubmitted 5 December 2019  
Accepted 29 January 2020  
10.1126/science.aaz5074



## Triple-halide wide-band gap perovskites with suppressed phase segregation for efficient tandems

Jixian XuCaleb C. BoydZhengshan J. YuAxel F. PalmstromDaniel J. WitterBryon W. LarsonRyan M. FranceJérémie WernerSteven P. HarveyEli J. WolfWilliam WeigandSalman ManzoorMaikel F. A. M. van HestJoseph J. BerryJoseph M. LutherZachary C. HolmanMichael D. McGehee

*Science*, 367 (6482), • DOI: 10.1126/science.aaz5074

### Tuning band gaps with three halides

Tandem solar cells can boost solar cell efficiency by using two active layers to absorb the solar spectrum more completely, provided that the two cells are current-matched. Inorganic-organic perovskites tuned to the appropriate wide band gap (#1.7 electron volts) as top cells that contained iodine and bromine or bromine and chlorine have short carrier diffusion lengths and undergo photo-induced phase segregation. Xu *et al.* now report a method for incorporating chloride that allows for fabrication of stable triple-halide perovskites with a band gap of 1.67 electron volts. Two-terminal tandem silicon solar cells made with this material had a power conversion efficiency of 27%.

*Science*, this issue p. 1097

### View the article online

<https://www.science.org/doi/10.1126/science.aaz5074>

### Permissions

<https://www.science.org/help/reprints-and-permissions>

Use of this article is subject to the [Terms of service](#)